

THERMAL MANAGEMENT

Simultaneous electrical and thermal rectification in a monolayer lateral heterojunction

Yufeng Zhang^{1†}, Qian Lv^{2†}, Haidong Wang^{1*}, Shuaiyi Zhao¹, Qihua Xiong^{3,4,5,6}, Ruitao Lv^{2,7*}, Xing Zhang^{1*}

Efficient waste heat dissipation has become increasingly challenging as transistor size has decreased to nanometers. As governed by universal Umklapp phonon scattering, the thermal conductivity of semiconductors decreases at higher temperatures and causes heat transfer deterioration under high-power conditions. In this study, we realized simultaneous electrical and thermal rectification (TR) in a monolayer MoSe₂-WSe₂ lateral heterostructure. The atomically thin MoSe₂-WSe₂ heterojunction forms an electrical diode with a high ON/OFF ratio up to 10⁴. Meanwhile, a preferred heat dissipation channel was formed from MoSe₂ to WSe₂ in the ON state of the heterojunction diode at high bias voltage with a TR factor as high as 96%. Higher thermal conductivity was achieved at higher temperatures owing to the TR effect caused by the local temperature gradient. Furthermore, the TR factor could be regulated from maximum to zero by rotating the angle of the monolayer heterojunction interface. This result opens a path for designing novel nanoelectronic devices with enhanced thermal dissipation.

The size of silicon chips has continuously decreased in recent decades and is approaching its physical limits. The electronics industry has been faced with the arduous challenge of finding nanomaterials with intrinsic semiconductor characteristics (1). To date, semiconductor carbon nanotubes (2), graphene nanoribbons (3), and transition-metal dichalcogenide (TMD) monolayers (4–13) have been promising candidates for next-generation field-effect transistors beyond silicon. Compared with carbon-based semiconductors, monolayer TMD materials have a direct electronic bandgap and a high ON/OFF ratio. In particular, monolayer TMD lateral heterostructures can form an atomic-scale p-n node to minimize the size of the diode channel, which has great potential in highly integrated electronics to further push the limit of Moore's law (6–15). However, miniaturization and high integration will inevitably lead to an increase in the heat flux density and a rapid increase in node temperature (16). Generally, owing to Umklapp phonon-phonon scattering, the thermal conductivity of semiconductor materials dominated by phonon transport will decrease as the temperature increases, which accelerates the thermal failure of high-

power density electronic devices (17–19). Designing a nanoscale electrical rectifier with a positive correlation between thermal conductivity and temperature that works above room temperature would be an ideal solution. Without external heat dissipation channels, more heat can be dissipated through the semiconductor material itself given its larger thermal conductivity at higher temperatures. However, no relevant experimental results have been reported thus far.

We fabricated a monolayer MoSe₂-WSe₂ lateral heterostructure device with simultaneous electrical rectification (ER) and thermal rectification (TR) characteristics, which were precisely measured by using a specially designed suspended H-type sensor. In the experiment, the monolayer MoSe₂-WSe₂ lateral heterojunction worked as an efficient electrical diode with a high ON/OFF ratio up to 10⁴. In the OFF state, the reverse saturation current was small, and the joule heating effect was negligible. No heat flux or temperature gradient was formed in the heterojunction diode, so there was no preferred direction for phonon transport. In the ON state with a large bias voltage, the high current caused a substantial joule heating effect in the heterojunction area, and, consequently, a temperature gradient was formed from the high-resistivity MoSe₂ domain to the low-resistivity WSe₂ domain. This happened to be the preferred direction for both phonon transport and electron migration in the heterojunction diode. The thermal conductivity was increased by 96% at maximum in the preferred phonon transport direction from MoSe₂ to WSe₂. Benefiting from the simultaneous ER and TR characteristics of monolayer lateral heterojunction, the atomically thin working electrical diode can achieve larger thermal conductivity at higher temperature owing to the local temperature gradient.

The TR effect of the MoSe₂-WSe₂ lateral heterojunction rectifier was experimentally demonstrated to be angle dependent. The largest TR factor was realized when phonons vertically crossed the heterojunction interface. If the phonon transport direction was parallel to the heterojunction interface, the TR effect vanished. Our molecular dynamics (MD) simulation result was consistent with the experimental data and indicated that the asymmetric heterojunction interface transport behavior triggered by lattice anharmonicity should be responsible for TR in lateral heterostructures. The simultaneous ER and TR characteristics of the two-dimensional MoSe₂-WSe₂ lateral heterostructure put forward a new design principle and the possibility of developing highly integrated electronic devices with better thermal dissipation performance.

Growth and device fabrication of MoSe₂-WSe₂ lateral heterostructures

The MoSe₂-WSe₂ lateral heterostructure samples were synthesized by an atmospheric-pressure chemical vapor deposition (AP-CVD) route with the assistance of gold foil (20). To simultaneously measure the ER and TR characteristics of the same lateral heterostructure sample, we designed an H-type sensor, as previously reported (20, 21). We supported the MoSe₂-WSe₂ heterostructure sample on a 300-nm-thick SiO₂ layer that bridges two gold nanosensors, forming an H-type structure (Fig. 1A). We used the gold sensor as an electrode, a joule heater, and a precise resistance thermometer simultaneously. We fully suspended the whole H-type sensing device from the silicon substrate to achieve the highest thermal measurement sensitivity. In the experiment, we could easily switch the electrical and thermal measurement modes by changing the outside electrical circuit.

We obtained atomic-resolution images of the MoSe₂, WSe₂, and interface domains, respectively, using high-angle annular dark-field scanning transmission electron microscopy (HAADF-STEM) (Fig. 1, B to D). The dark and bright dots in each HAADF-STEM image denote Mo and W atoms, respectively. We drew a polyline (indicated by the yellow dashed line) to indicate the shape of the heterojunction interface (Fig. 1D). We observed slight doping at the interface, which might be due to the relatively high energy at the interface region. By counting the number of Mo and W atoms in the HAADF-STEM image, we estimated the doping concentration to be ~10% for our tested samples. We selected six samples, labeled 1 to 6, for electrical and thermal measurements and showed their initial configurations (Fig. 1, E to J). With the help of a prefabricated micrometer-sized cross mark array and the automatic identification and positioning function of the electron beam lithography system,

¹Key Laboratory for Thermal Science and Power Engineering of Ministry of Education, Department of Engineering Mechanics, Tsinghua University, Beijing 100084, China.

²State Key Laboratory of New Ceramics and Fine Processing, School of Materials Science and Engineering, Tsinghua University, Beijing 100084, China. ³State Key Laboratory of Low-Dimensional Quantum Physics and Department of Physics, Tsinghua University, Beijing 100084, China.

⁴Frontier Science Center for Quantum Information, Beijing 100084, China. ⁵Collaborative Innovation Center of Quantum Matter, Beijing 100084, China. ⁶Beijing Academy of Quantum Information Sciences, Beijing 100193, China. ⁷Key Laboratory of Advanced Materials (Ministry of Education), School of Materials Science and Engineering, Tsinghua University, Beijing 100084, China.

*Corresponding author. Email: hdwang@tsinghua.edu.cn (H.W.); lvruitao@tsinghua.edu.cn (R.L.); x-zhang@tsinghua.edu.cn (X.Z.)

†These authors contributed equally to this work.

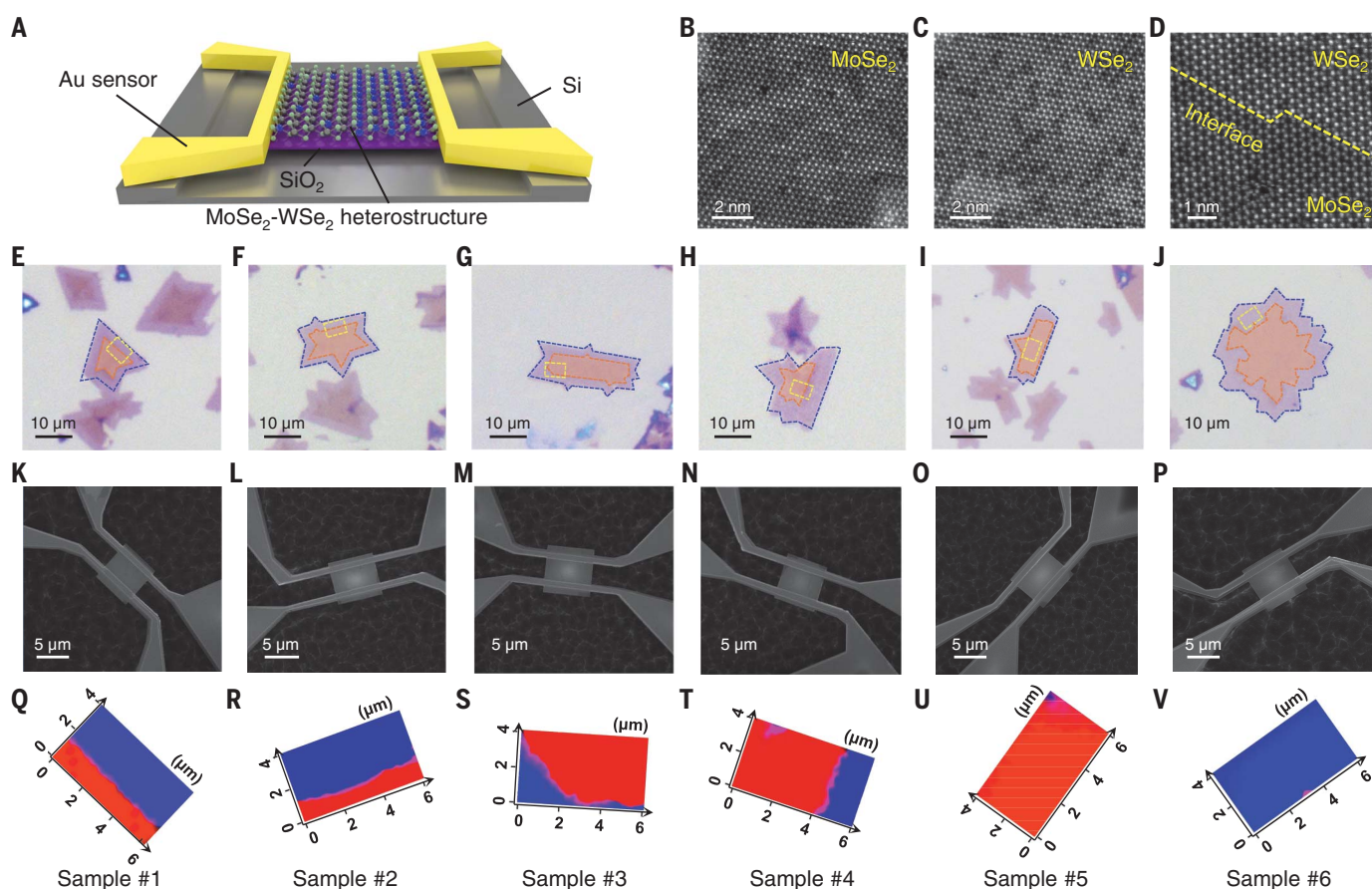


Fig. 1. Characterization of as-synthesized MoSe₂-WSe₂ lateral heterostructures and fabricated H-type sensing devices. (A) Schematic diagram of the suspended H-type sensing device. (B to D) Atomic-resolution HAADF-STEM images of MoSe₂, WSe₂, and the interface domain, respectively. (E to J) Optical micrograph images of samples 1 to 6 synthesized on SiO₂/Si substrates with MoSe₂ (dark contrast, outlined in orange dashed lines) surrounded by WSe₂ (bright contrast, outlined in blue dashed lines).

The yellow dashed boxes show the sample areas prepared for characteristic measurement. (K to P) SEM images of samples 1 to 6 fabricated into H-type sensing devices, which are fully suspended from the silicon substrate with an etching depth of 8 μm to avoid heat loss into the substrate. (Q to V) Raman spatial mapping images of samples 1 to 6. The red, blue, and pink colors represent the MoSe₂, WSe₂, and interface domains, respectively. Raman spectra of the representative domains can be found in fig. S1.

we were able to precisely select the lateral heterojunction area and place it at the center between two gold nanosensors, with a spatial accuracy better than 100 nm. Each freestanding rectangle area between two sensors (Fig. 1, K to P) corresponds to the lateral heterojunction sample marked by yellow dashed boxes (Fig. 1, E to J). Using a high-resolution Raman spectrometer, we scanned all six suspended heterojunction samples and obtained Raman spectral mapping images (Fig. 1, Q to V, and fig. S1). We verified the uniformity of the as-synthesized heterostructure samples with the Raman mapping results. The shape of the MoSe₂-WSe₂ heterojunction interface is clearly illustrated in the Raman spectral mapping images, which are consistent with our initial optical micrograph images. We defined θ as the angle between the length directions of the interface and the elongated H-type sensors. When the interface is parallel to the sensor, $\theta = 0^\circ$ (samples 1 and 2), and the electrons or phonons flow perpendicularly through the interface. Otherwise, when the interface and

sensor are perpendicular to each other, $\theta = 90^\circ$ (sample 4), and the electrons or phonons flow parallel to the interface. In addition to θ of 0° and 90° , sample 3 has an angle θ of 45° (fig. S2), and samples 5 and 6 are pure MoSe₂ and pure WSe₂, respectively. We measured these three samples to study the interface angle dependence and as control samples to verify the reliability of the experimental results.

Electrical characterization

We used the four-probe method to characterize the electrical transport across the interface (Fig. 2A). The measurement system included a precise dc voltage and current source (ADCM, 6243), two high-precision digital multimeters (Keithley 2002, 8 $\frac{1}{2}$ -digits), and a vacuum thermoelectric heating and cooling stage (INSTEC, TP102SV-PM-F8, ± 0.001 K). We measured the drain-source current-drain-source voltage ($I_{\text{ds}}-V_{\text{ds}}$) curves of four MoSe₂-WSe₂ lateral heterostructure samples and pure MoSe₂, pure WSe₂ samples under zero back-gate voltage

(Fig. 2, B to F). The n-type MoSe₂ and p-type WSe₂ form a natural p-n junction with type-II band alignment at the interface. We show a sketch of the band alignment of MoSe₂ and WSe₂ domains when forming the heterojunction (Fig. 2B, inset). We obtained the bandgaps directly with the photoluminescence measurement (fig. S3). For samples 1, 2, and 3, the lateral p-n junction interface is located in the path of carrier transport from the source to the drain, and, as a consequence, the $I_{\text{ds}}-V_{\text{ds}}$ curve shows a clear diode response. This electrical current rectification behavior cannot be attributed to the Schottky barriers of metallic electrode contacts, given the symmetric $I_{\text{ds}}-V_{\text{ds}}$ curves of individual MoSe₂ and WSe₂ (Fig. 2F). The high ER ratio of 10^3 to 10^4 in samples 1 and 2 proves the high interface quality of the as-synthesized MoSe₂-WSe₂ lateral heterostructures. However, the ER ratio of sample 3 is substantially lower in comparison. This behavior is due to the tilted interface structure, which can be regarded as a parallel connection between a heterostructure and pure MoSe₂.

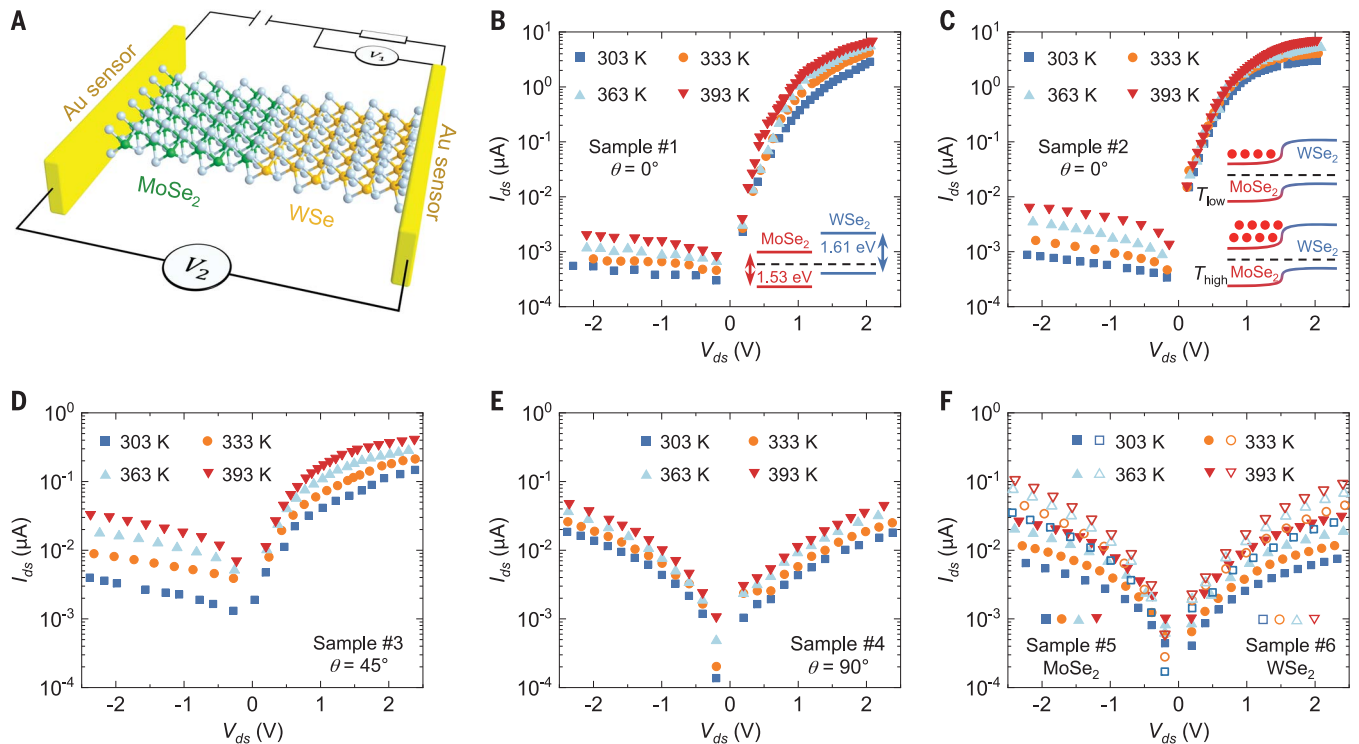


Fig. 2. External electrical measurement circuit and thermodynamic characterization of the electrical properties of MoSe₂-WSe₂ lateral heterostructures.

(A) Schematic diagram of the electrical measurement circuit based on the H-type device, where the MoSe₂-WSe₂ heterostructure sample is in contact with two gold sensors, and one multimeter, V_1 , is used to measure the voltage and another

multimeter, V_2 , is used to measure the current through the heterostructure sample. I_{ds} - V_{ds} characterization of (B) sample 1, (C) sample 2, (D) sample 3, (E) sample 4, and (F) samples 5 and 6 at different temperatures ranging from 303 to 393 K. Insets in (B) and (C) are sketches of the band alignments and the thermionic effect in the MoSe₂-WSe₂ lateral heterostructure, respectively.

Furthermore, we studied the thermodynamic behavior of charge carriers by varying the temperature from 303 to 393 K. A temperature dependence can be found in the I_{ds} - V_{ds} curves of all measured samples. Both the temperature-dependent current and rectification ratio are related to the interface angle. For heterostructure samples 1 to 3, forward current monotonically increases with temperature owing to the increase of thermionic emission. More electrons can contribute to the forward current when temperature is raised (Fig. 2C, inset). For the reverse bias conditions, more electron-hole pairs are generated in the depletion region because of the increase in kinetic energy at high temperature, thus leading to an increase trend of reverse current. In addition, the temperature influence on the reverse generation current is more pronounced than that on the forward current, resulting in a reduction of ER ratio. For samples 4 to 6 lacking the built-in potential, both the forward and reverse currents also increase with temperature because of the enhancement of carrier concentration. The symmetric I_{ds} - V_{ds} curves at different temperatures indicate the absence of an ER effect.

Thermal rectification measurement

We used the H-type sensor method to measure the thermal conductivities of the monolayer

MoSe₂-WSe₂ lateral heterostructure in two opposite heat flow directions (21–23). We performed all the experiments in a high-vacuum chamber (pressure $< 10^{-3}$ Pa), and the heat loss due to convection and thermal irradiation could be safely neglected [see (20) for detailed uncertainty analysis]. Furthermore, as seen in the scanning electron microscopy (SEM) images (Fig. 1, K to P), the geometric size of the gold sensor (0.8 μm in width, 15 μm in length, and 100 nm in thickness) was much smaller than that of the MoSe₂-WSe₂ heterostructure (6 μm in width and 4 μm in length) supported on a 300-nm-thick SiO₂ layer. The suspended gold sensor could offer high sensitivity in temperature measurement as a precise resistance thermometer. The influences of the contact thermal resistance between the gold sensor and two-dimensional (2D) material were carefully considered [see (20) for discussion]. Given the relatively large thermal resistance of the tested sample, we neglected the influence of the contact thermal resistance.

We heated one gold sensor and used the other one to detect the temperature rise (Fig. 3A). The heat flow direction can be reversed by exchanging the roles of “heater” and “detector” between the two sensors (20) (fig. S4). Because of the relatively weak mechanical strength of TMD materials (24), a thin supporting SiO₂

layer is essential to avoid device failure. We considered the influence of the supporting SiO₂ layer on the thermal property characterization of the MoSe₂-WSe₂ monolayer (20), which has no effect on the temperature difference between the two gold sensors in the experiment.

We plotted the measured thermal conductivities (table S1) of six samples (Fig. 3, B to F). The measured thermal conductivities (λ) of homogeneous MoSe₂ (sample 5) and WSe₂ (sample 6) are 45 and 40 W/(m·K) at room temperature, which is consistent with the literature values (25, 26), proving the measurement accuracy of the H-type method. The flattened tendency of the thermal conductivity versus temperature curve was attributed to the atomic doping and SiO₂ substrate-induced phonon scattering, which is ubiquitous in monolayer 2D materials (27, 28). The λ discrepancies of homogeneous MoSe₂ and WSe₂ in different heat flow directions are $< 3\%$, showing no TR effect, as expected. We show the thermal conductivities of MoSe₂-WSe₂ heterostructure samples 1 and 2, where the heterojunction interface is vertical to the heat flow direction ($\theta = 0^\circ$) (Fig. 3, B and C). In the heat flow direction from MoSe₂ to WSe₂ (the J^+ direction), sample 1 has a λ of ~ 30 W/(m·K) at 273 K, which is 96% higher than that in the opposite direction. Sample 2 has a TR factor

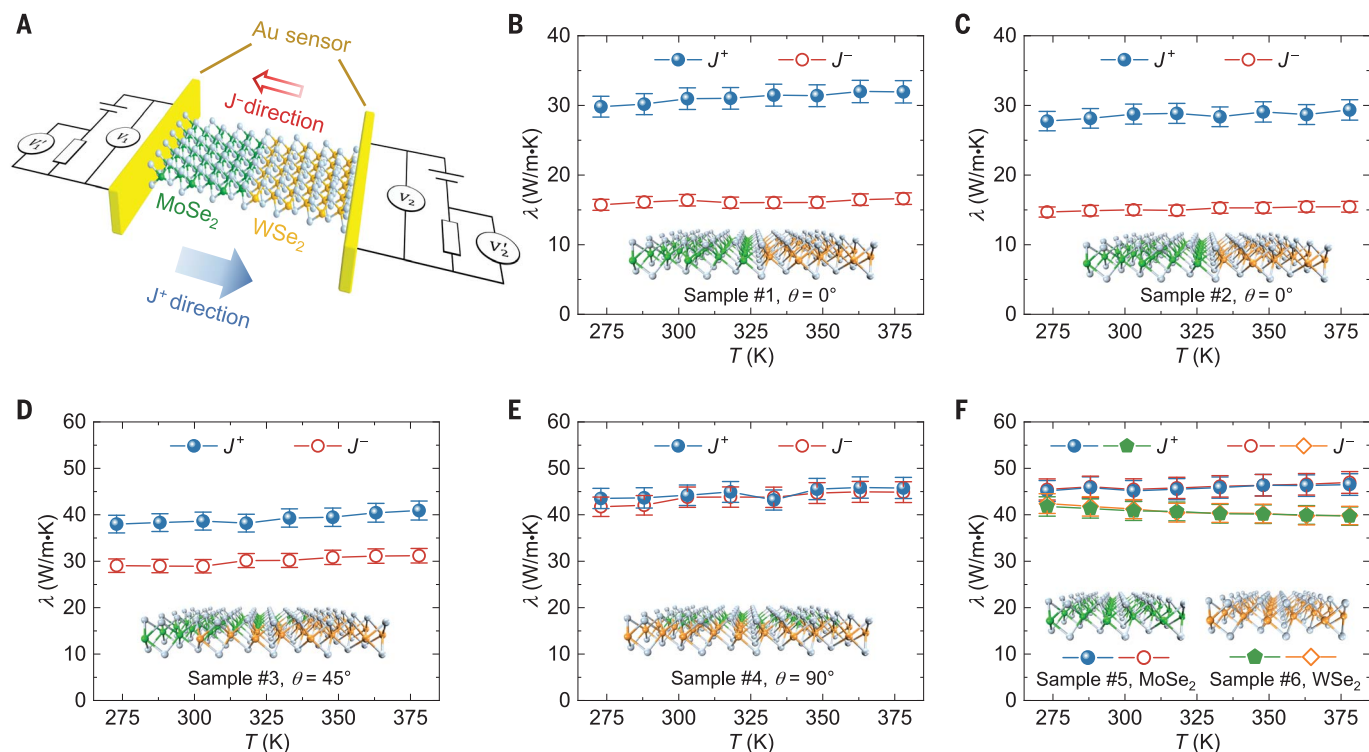


Fig. 3. External thermal measurement circuit and TR characteristics of MoSe₂-WSe₂ lateral heterostructures. (A) Schematic diagram of the thermal measurement circuit based on the H-type sensing device. Two precision dc power supplies, two standard resistors, and four high-precision digital multimeters are built in, where V₁ and V₂ are used to measure the voltages of the two gold sensors, and V₁' and V₂' are used to measure the current (divided by the standard resistance) in each loop. The blue solid arrow represents the high thermal conductivity direction J⁺ from MoSe₂ to WSe₂, while the red hollow arrow

represents the low thermal conductivity direction J⁻ from WSe₂ to MoSe₂. (B to F) The measured thermal conductivities of samples 1 to 6, respectively, in two opposite heat flow directions within a temperature range of 273 to 378 K. The insets show the atomic diagrams to demonstrate the interface morphology features at different angles. In each figure, the blue symbols represent the thermal conductivity in J⁺ direction, while the red symbols represent the thermal conductivity in J⁻ direction. Error bars show experimental uncertainties of ±5%.

of 93%, consistent with the result of sample 1, owing to their similar heterojunction morphologies illustrated in the Raman spatial mapping images (Fig. 1, Q and R). For sample 3, the heat flows obliquely across the heterojunction interface at θ = 45°, and the TR factor is 32% (Fig. 3D). For sample 4, the heterojunction interface is parallel to the heat flow direction (θ = 90°), and the TR effect vanishes (Fig. 3E). The experimental results demonstrate that the TR effect is dependent on the angle between the heterojunction interface and heat flow direction. By simply adjusting the angle θ, the TR factor can be regulated between its maximum and zero. This provides an effective way to actively control phonon transport in monolayer heterostructures.

In reality, the existence of TR in the heterostructure could be directly proven from the original experimental data of the resistance of the H-type sensor in different heat flow directions (table S2). For monolayer heterostructure sample 1, the temperature of the detector sensor was 2.62 K higher in the J⁺ direction than in the J⁻ direction at a fixed temperature rise of 30 K at the heater sensor (fig. S6). In

contrast, for the homogeneous MoSe₂ sample 5, the temperature rise relationship between the detector sensor and heater sensor was the same in both the J⁺ and J⁻ directions. This observation is solid proof of TR without any possible changes caused by finite element analysis or data postprocessing.

Furthermore, the thermal conductivities of heterostructure samples 1, 2, and 3 show a slight increasing trend with increasing temperature. This trend has been theoretically predicted to be the consequence of the increasing interfacial thermal conductance of a two-segment heterostructure system owing to the increase in phonon transmission caused by the enhanced anharmonicity at the inelastic interface (29). The agreement between the measurement and theoretical prediction further verifies the accuracy and reliability of our experimental data and proves the interface-dominated phonon transport in the MoSe₂-WSe₂ heterostructure.

Understanding the mechanisms of the TR effect

Given that previous experiments proved that the electron-dominated thermal rectifiers can

have an ultrahigh TR ratio of up to 140 at low temperature (30, 31), the intrinsic electrical diode effect of the lateral heterostructure prompted us to first look into the role of electrons. We performed a thorough examination and found that the electronic thermal conductivity is negligible in the MoSe₂-WSe₂ lateral heterostructure (20) (fig. S7), which means that phonons are the main heat carriers. We performed a nonequilibrium molecular dynamics (NEMD) simulation to reveal the physical mechanisms of TR. We started with a schematic diagram of the MoSe₂-WSe₂ lateral heterostructure divided into segments of pure materials (I and III) and interface (II) (Fig. 4A). Our simulation results indicate that heat preferentially flows from the MoSe₂ domain to the WSe₂ domain, consistent with the experimental results. Given the small contribution of the temperature-dependent thermal conductivities of individual MoSe₂ and WSe₂ to the TR effect (20), we turned to examine the phonon spectra mismatch of regions I and III in both the J⁺ and J⁻ directions (Fig. 4B). When heat flows in the J⁺ direction from MoSe₂ to WSe₂, the phonon spectra of the MoSe₂ and WSe₂ domains match

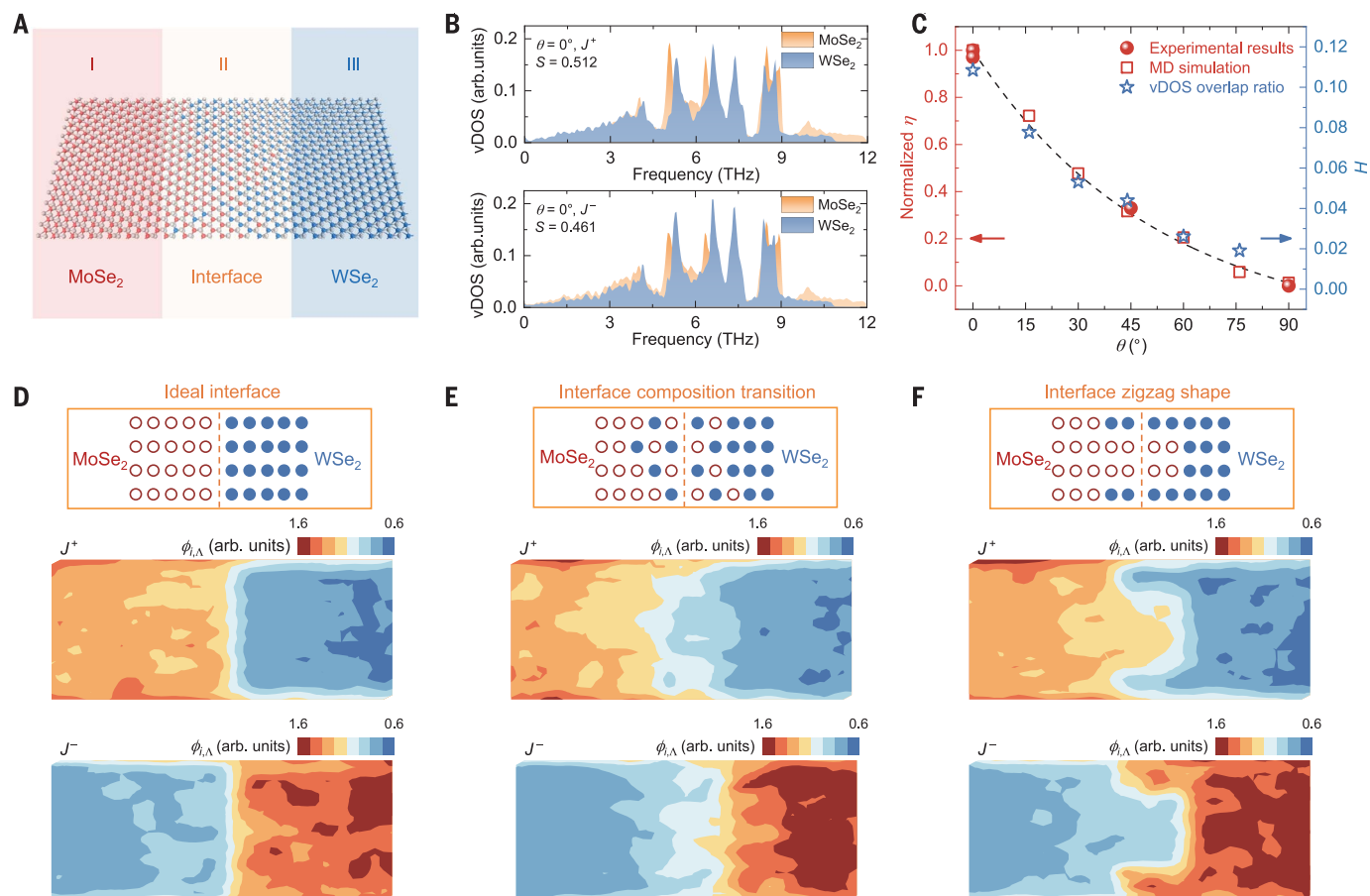


Fig. 4. MD simulation results revealing the physical mechanisms of TR.

(A) Schematic diagram of the MoSe₂-WSe₂ lateral heterostructure models built for MD simulation with pure materials (I and III) and interface (II). (B) Vibrational density of states (vDOS) for $\theta = 0^\circ$ in two directions. The larger spectra overlap (S) in the J^+ direction indicates higher thermal conductance across the interface.

(C) Normalized TR ratio (η) and spectra overlap ratio (H) plotted with angle (θ). Schematic diagrams and distribution of localized phonon modes in forward and reverse directions for three different interface morphologies: (D) an ideal interface, (E) a composition transition interface, and (F) a zigzag-shaped interface. arb. units, arbitrary units.

well at low frequency (<4 THz). The coupling phonons with long wavelengths serving as the major force of heat conduction facilitate thermal transport across the interface. In contrast, the phonon spectra are staggered in the reverse J^- direction from WSe₂ and MoSe₂, which hinders the transmission of lattice vibrational energy across the interface. We further calculated the spectra overlap (S) to quantify the matching of the phonon bands. The overlap S^+ and S^- are 0.512 and 0.461 in the J^+ and J^- directions, respectively. A larger spectra overlap corresponds to a higher thermal conductivity, as observed in the experiment. A clearer physical picture of TR can be seen from the spatial energy distribution of propagating phonon modes (fig. S8).

In addition to the theory of phonon spectra overlap, another factor derived from the interface morphology also contributes to the TR effect. The HAADF-STEM image (Fig. 1D) shows the actual interface with a zigzag shape and compositional transition. A more precise model including region II was built, and the

simulation results indicated that the real zigzag-shaped interface with local compositional transition enhances the TR effect (fig. S9). We also computed the distribution of localized phonon modes (Fig. 4, D to F), and the results demonstrated that the exchange between Mo and W atoms and narrow edges induced by the zigzag structure at the interface cause more localized phonon modes in the J^- direction (appearing dark red). This enhances the TR effect on the basis of the ideal sharp interface (Fig. 4D). The overlap of phonon spectra can be used to explain the mechanism of the TR effect caused by phonon anharmonicity of two dissimilar materials, while the composition transition and zigzag structure at the interface can further enhance the TR effect. The combination of these two mechanisms together results in a high TR ratio of 96% in monolayer MoSe₂-WSe₂ heterojunctions.

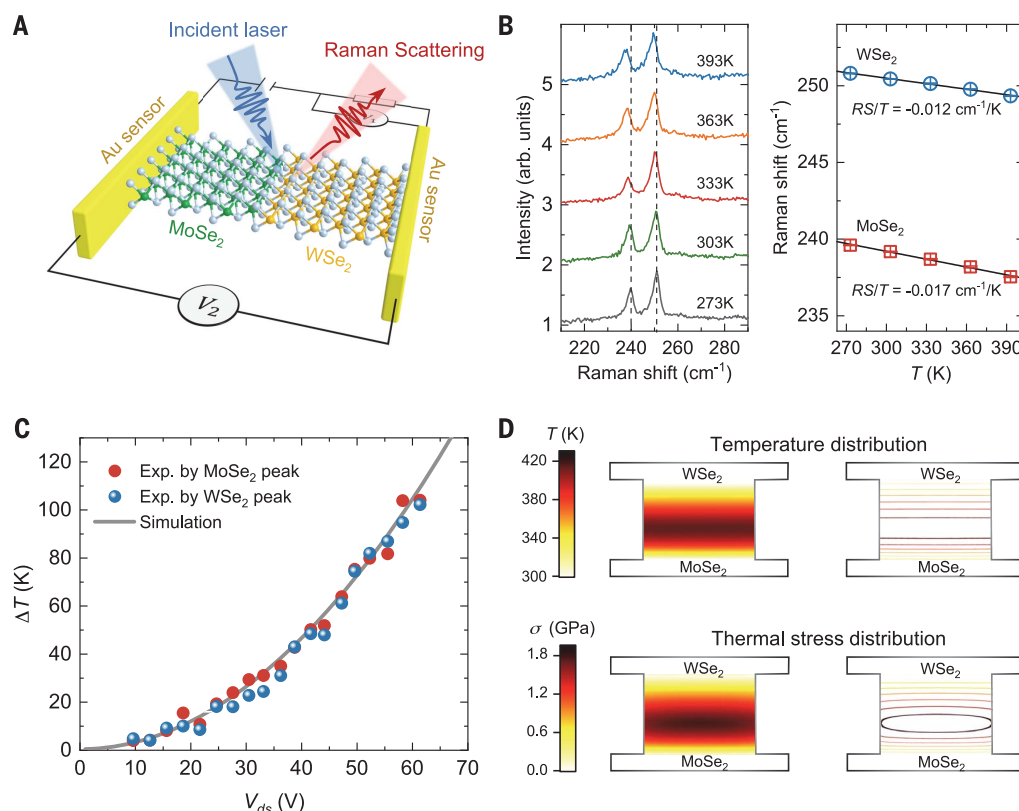
Our experimental results demonstrate that the TR ratio of the MoSe₂-WSe₂ heterostructure can be regulated by changing the angle

between the directions of the interface and heat flow. To explain the angle-dependent TR effect, we set up seven different models with angle θ varying from 0° to 90° and separately calculated their TR ratios, phonon spectra, and spatial energy distribution (figs. S8, S10, and S11). The results show that the TR ratio monotonically decreases with increasing angle θ and finally disappears when the interface is parallel to the heat flow direction (Fig. 4C), consistent with the experimental results [see (20) for detailed discussion].

Numerous studies have demonstrated that the essence of TR is the asymmetry of phonon transport in the asymmetric structure (21, 32–45). For homogeneous materials, TR can be achieved by artificially cutting or kneading the sample into asymmetric shapes, such as trapezoidal or T-shaped graphene (21, 43) and diamond nanopillars (42). In this case, TR originates from phonon lateral confinement and vanishes at the macroscale. The as-synthesized MoSe₂-WSe₂ heterostructure is a typical two-segment system with inherent

Fig. 5. High-bias voltage experiment of the heterostructure with temperature characterization by Raman spectroscopy. (A) Schematic diagram of the temperature measurement.

The MoSe₂-WSe₂ heterostructure was heated by an electrical current, and the temperature was measured by the Raman shift. (B) Calibration of the temperature-dependent Raman shift for WSe₂ and MoSe₂ segments from 273 to 393 K. The linearly fitted values of the slope are $-0.012 \text{ cm}^{-1}/\text{K}$ and $-0.017 \text{ cm}^{-1}/\text{K}$ for representative Raman peaks of WSe₂ and MoSe₂, respectively. Error bars show experimental uncertainties of eight individual measurements. (C) Temperature rise measured by experiment and calculated from finite element analysis. The laser beam was focused at the heterostructure interface, and the local temperature rise was obtained through the Raman shifts of both MoSe₂ and WSe₂ peaks. (D) Comparison of the asymmetric temperature and thermal stress distributions of the H-type device at $V_{\text{ds}} = 60 \text{ V}$.



asymmetric structure, different from the previous examples. The interface formed by the covalent bonding between two materials acts as a sluice gate for both electron and phonon flows. When the size of the system increases, the role of the interface is suppressed, thus leading to a declining trend in the TR effect (fig. S12). However, the TR effect will not vanish in heterostructure as long as the interface exists.

Application

In practical applications, the applied bias voltage is much larger than that in our property measurements. To verify the upper limit of endurable bias voltage and corresponding temperature rise of the p-n heterojunction diode device, we measured the temperature rise at the interface by using noncontact Raman spectroscopy while continuously increasing the forward bias voltage to the MoSe₂-WSe₂ diode (Fig. 5A). The temperature dependence of the Raman shift was calibrated beforehand, and a small laser power was used so that the temperature rise caused by laser heating could be neglected. We show the A_{1g} mode peaks of both MoSe₂ and WSe₂, displaying a remarkable redshift with increasing temperature (Fig. 5B). We can fit the Raman shift versus temperature by a linear function with a slope of $-0.017 \text{ cm}^{-1}/\text{K}$ for the MoSe₂ A_{1g} mode and $-0.012 \text{ cm}^{-1}/\text{K}$ for the WSe₂ A_{1g} mode, agree-

ing well with the literature values (25, 26). In the experiment, the bias voltage (V_{ds}) was gradually increased from 0 V to the maximum 61 V, at which point the diode device broke down. Figure 5C shows the measured temperature rise at the interface through the Raman shifts of both the MoSe₂ A_{1g} mode and WSe₂ A_{1g} mode peaks. The results from the two representative peak shifts show good agreement with each other, verifying the accuracy and reliability of Raman spectra measurement. Figure 5D depicts the asymmetric temperature and thermal stress distributions of the heterostructure device calculated by COMSOL.

The maximum current density of the monolayer heterojunction was estimated to exceed $2 \times 10^7 \text{ A}/\text{cm}^2$, and the local temperature rise at the interface was measured to be 100 K before breakdown. The severe electromigration damage induced by high current density and high temperature at the interface is the main reason for the breakdown of the heterojunction device (46). The high local thermal stress further aggravates the damage. Therefore, decreasing the local temperature at heterojunction interface is the key factor to mitigate the electromigration damage and reduce the thermal stress, prolonging the life of the device. Benefiting from the TR effect, the lateral heterostructure has higher thermal conductivity in the ON state, which facilitates the heat

dissipation and decreases the temperature at interface.

Conclusions

For highly integrated circuits at the nanoscale, efficient heat dissipation is crucial for better device performance and extended lifetime. Unfortunately, the universal Umklapp phonon-phonon scattering near room temperature causes a negative correlation between thermal conductivity and temperature, leading to heat transfer deterioration in high-power integrated circuits. In this work, we fabricated a monolayer MoSe₂-WSe₂ heterostructure device that possesses simultaneous ER and TR characteristics. This atomically thin electrical diode has a high ON/OFF ratio up to 10^4 . When it works as a diode in the ON state with a large bias voltage, the thermal conductivity of device is increased by 96% in the heat flow direction from MoSe₂ to WSe₂. The monolayer lateral heterostructure has an enhanced capability to remove wasted heat by itself without external heat dissipation channels. This finding paves a new way for designing heterostructure devices with better electrical and thermal performances simultaneously.

REFERENCES AND NOTES

1. H. N. Khan, D. A. Hounshell, E. R. H. Fuchs, *Nat. Electron.* **1**, 14–21 (2018).
2. G. Hills et al., *Nature* **572**, 595–602 (2019).
3. J. P. Llinas et al., *Nat. Commun.* **8**, 633 (2017).

4. B. Radisavljevic, A. Radenovic, J. Brivio, V. Giacometti, A. Kis, *Nat. Nanotechnol.* **6**, 147–150 (2011).
5. J. G. Song *et al.*, *ACS Nano* **7**, 11333–11340 (2013).
6. Y. Gong *et al.*, *Nat. Mater.* **13**, 1135–1142 (2014).
7. X. Duan *et al.*, *Nat. Nanotechnol.* **9**, 1024–1030 (2014).
8. Y. Gong *et al.*, *Nano Lett.* **15**, 6135–6141 (2015).
9. M. Y. Li *et al.*, *Science* **349**, 524–528 (2015).
10. P. K. Sahoo, S. Memaran, Y. Xin, L. Balicas, H. R. Gutiérrez, *Nature* **553**, 63–67 (2018).
11. J. Zhu *et al.*, *J. Am. Chem. Soc.* **142**, 16276–16284 (2020).
12. Y. Yoo, Z. P. Degregorio, J. E. Johns, *J. Am. Chem. Soc.* **137**, 14281–14287 (2015).
13. C. Huang *et al.*, *Nat. Mater.* **13**, 1096–1101 (2014).
14. Z. Zhang *et al.*, *Science* **357**, 788–792 (2017).
15. S. Xie *et al.*, *Science* **359**, 1131–1136 (2018).
16. A. L. Moore, L. Shi, *Mater. Today* **17**, 163–174 (2014).
17. N. Mingo, *Phys. Rev. B* **68**, 113308 (2003).
18. T. L. Feng, X. L. Ruan, *Phys. Rev. B* **93**, 045202 (2016).
19. T. L. Feng, L. Lindsay, X. L. Ruan, *Phys. Rev. B* **96**, 161201 (2017).
20. Materials and methods are available as supplementary materials.
21. H. Wang *et al.*, *Nat. Commun.* **8**, 15843 (2017).
22. S. Fujiwara, X. Zhang, M. Fujii, *High Temp. High Press.* **33**, 271–278 (2001).
23. S. Y. Zhao, H. D. Wang, *ES Energy & Environment* **9**, 59–66 (2020).
24. K. Liu, J. Q. Wu, *J. Mater. Res.* **31**, 832–844 (2016).
25. X. Zhang *et al.*, *ACS Appl. Mater. Interfaces* **7**, 25923–25929 (2015).
26. E. Easy *et al.*, *ACS Appl. Mater. Interfaces* **13**, 13063–13071 (2021).
27. J. H. Seol *et al.*, *Science* **328**, 213–216 (2010).
28. M. An, D. S. Chen, W. G. Ma, S. Q. Hu, X. Zhang, *Int. J. Heat Mass Transf.* **178**, 121630 (2021).
29. X. Liu, J. Gao, G. Zhang, Y. W. Zhang, *Nanoscale* **10**, 19854–19862 (2018).
30. F. Giazotto, F. S. Bergeret, *Appl. Phys. Lett.* **103**, 242602 (2013).
31. M. J. Martínez-Pérez, A. Fornieri, F. Giazotto, *Nat. Nanotechnol.* **10**, 303–307 (2015).
32. N. B. Li *et al.*, *Rev. Mod. Phys.* **84**, 1045–1066 (2012).
33. N. A. Roberts, D. G. Walker, *Int. J. Therm. Sci.* **50**, 648–662 (2011).
34. C. W. Chang, D. Okawa, A. Majumdar, A. Zettl, *Science* **314**, 1121–1124 (2006).
35. B. Liang, X. S. Guo, J. Tu, D. Zhang, J. C. Cheng, *Nat. Mater.* **9**, 989–992 (2010).
36. W. Kobayashi, Y. Teraoka, I. Terasaki, *Appl. Phys. Lett.* **95**, 171905 (2009).
37. R. Shrestha *et al.*, *Nat. Commun.* **11**, 4346 (2020).
38. X. Yang *et al.*, *ACS Appl. Mater. Interfaces* **12**, 28306–28312 (2020).
39. B. Li, L. Wang, G. Casati, *Phys. Rev. Lett.* **93**, 184301 (2004).
40. B. Li, J. Lan, L. Wang, *Phys. Rev. Lett.* **95**, 104302 (2005).
41. N. Yang, N. Li, L. Wang, B. Li, *Phys. Rev. B* **76**, 020301 (2007).
42. J. Lee, V. Varshney, A. K. Roy, J. B. Ferguson, B. L. Farmer, *Nano Lett.* **12**, 3491–3496 (2012).
43. Y. Wang *et al.*, *Nano Lett.* **14**, 592–596 (2014).
44. X. K. Chen, Z. X. Xie, W. X. Zhou, L. M. Tang, K. Q. Chen, *Carbon* **100**, 492–500 (2016).
45. Y. Y. Zhang, Q. X. Pei, C. M. Wang, C. H. Yang, Y. W. Zhang, *J. Phys. Chem. C* **122**, 22783–22789 (2018).
46. D. Lembke, A. Kis, *ACS Nano* **6**, 10070–10075 (2012).

ACKNOWLEDGMENTS

Funding: H.W. acknowledges financial support from the National Natural Science Foundation of China (51976096). X.Z. acknowledges financial support from the National Natural

Science Foundation of China (51827807 and 52130602). R.L. acknowledges financial support from the National Key Research and Development Program of China (2021YFA1200800) and the National Natural Science Foundation of China (51972191). **Author contributions:** H.W., R.L., and X.Z. conceived of and designed the research. Q.L. grew the MoSe₂-WSe₂ lateral heterostructures and performed the high-resolution transmission electron microscopy characterization. H.W. designed and fabricated the H-type sensing devices. H.W. and Y.Z. performed the electrical and thermal property measurements and conducted Raman spectral mapping and high bias voltage measurements. Y.Z. conducted the molecular dynamics simulations. H.W. and S.Z. analyzed the data and performed the finite element simulations. H.W., Y.Z., and Q.L. wrote the manuscript with contributions from all authors. Q.X. provided valuable suggestions and revised the manuscript. **Competing interests:** The authors declare that they have no competing interests. **Data and materials availability:** All data are available in the main text or the supplementary materials. **License information:** Copyright © 2022 the authors, some rights reserved; exclusive licensee American Association for the Advancement of Science. No claim to original US government works. <https://www.science.org/about/science-licenses-journal-article-reuse>

SUPPLEMENTARY MATERIALS

science.org/doi/10.1126/science.abq0883
Materials and Methods
Supplementary Text
Figs. S1 to S14
Tables S1 to S4
References (47–64)

Submitted 17 March 2022; accepted 20 September 2022
10.1126/science.abq0883